

Jianjian Wang

State Key Laboratory of Tribology,
Tsinghua University,
Beijing 100084, China;
Department of Mechanical and
Automation Engineering,
The Chinese University of Hong Kong,
Hong Kong 999077, China

Jianfu Zhang

State Key Laboratory of Tribology,
Tsinghua University,
Beijing 100084, China

Pingfa Feng¹

State Key Laboratory of Tribology,
Tsinghua University,
Beijing 100084, China;
Division of Advanced Manufacturing,
Graduate School at Shenzhen,
Tsinghua University,
Shenzhen 518055, China

Ping Guo

Department of Mechanical and
Automation Engineering,
The Chinese University of Hong Kong,
Hong Kong 999077, China

Qiaoli Zhang

State Key Laboratory of Tribology,
Tsinghua University,
Beijing 100084, China

Feasibility Study of Longitudinal–Torsional-Coupled Rotary Ultrasonic Machining of Brittle Material

In order to further improve the processing performance of rotary ultrasonic machining (RUM), a novel longitudinal–torsional-coupled (LTC) vibration was applied to the RUM. An experimental study on quartz glass was performed to access the feasibility of the LTC-RUM of a brittle material. The LTC-RUM was executed through the addition of helical flutes on the tool of conventional longitudinal RUM (Con-RUM). The experimental results demonstrated that the LTC-RUM could reduce the cutting force by 55% and the edge chipping size at the hole exit by 45% on an average, compared to the Con-RUM. Moreover, the LTC-RUM could also improve the quality of the hole wall through the reduction of surface roughness, in particular, when the spindle speed was relatively low. The mechanism of superior processing performance of LTC-RUM involved the corresponding specific moving trajectory of diamond abrasives, along with higher lengths of lateral cracks produced during the abrasives indentation on the workpiece material. The higher edge chipping size at the hole entrance of LTC-RUM indicated a higher length of lateral cracks in LTC-RUM, due to the increase in the maximum cutting speed. Furthermore, the effect of spindle speed on the cutting force and surface roughness variations verified the important role of the moving trajectory of the diamond abrasive in the superior processing performance mechanism of LTC-RUM. [DOI: 10.1115/1.4038728]

Keywords: rotary ultrasonic machining, longitudinal–torsional composite vibration, hard and brittle material machining, hole manufacturing

1 Introduction

Brittle materials, represented by optical glass, advanced ceramics, and ceramic matrix composites, have been widely applied to many industries such as aeronautics, astronautics, medical appliances, automobile, and energy [1]. Numerous potential demands for brittle materials are attributed to their superior mechanical and chemical properties, such as high hardness, good wear resistance, and corrosion resistance [2]. In contrast, due to the high hardness and low fracture toughness, brittle materials are generally considered as the most difficult-to-machine materials [3]. Metal cutting technologies are not suitable for the processing of brittle material due to severe tool wear and machining induced damages. High efficiency and low damage machining solution for brittle materials is still a research hotspot in the field of material processing technology [4]. Till date, various traditional and non-traditional machining methods have been introduced for brittle material processing, such as grinding [5,6], ultrasonic vibration assisted grinding [7], laser machining [8,9], electrical discharge machining [10], abrasive water jet cutting [11], ultrasonic machining (USM) [12–14], and rotary ultrasonic machining (RUM) [15].

Figure 1 illustrates that in RUM, a rotating electroplated diamond core tool vibrates ultrasonically with tiny amplitude, simultaneously feeding toward the workpiece [16]. The RUM has been sufficiently proved as a superior method for hole manufacturing on brittle materials with reduced cutting force [17] and improved hole exit quality [18], consequently improving the drilling

efficiency compared to the grinding and USM. In order to maximize the processing superiorities of RUM for hole manufacturing on brittle materials, extensive research efforts have been devoted to investigate the removal mechanism of the corresponding material [19–21], processing performance [22–25] and modeling

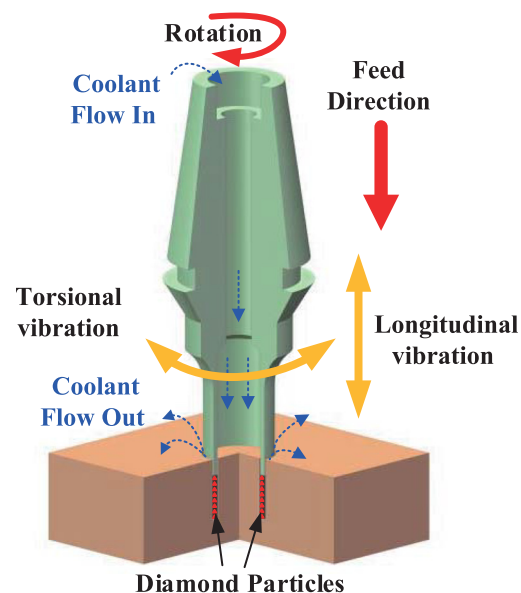


Fig. 1 Illustration of RUM

¹Corresponding author.

Manuscript received July 6, 2017; final manuscript received November 29, 2017; published online March 6, 2018. Assoc. Editor: Guillaume Fromentin.

[26–34], damage formation mechanism [35,36], and suppression methods [37–41]. The processing inputs utilized for performance optimization of RUM include the tool parameters, the cooling condition, the spindle speed, the feedrate, and the ultrasonic amplitude [42]. The mode of ultrasonic vibration also ought to be an important input variable of RUM [43]. In contrast, currently in most of the reported research regarding RUM, the ultrasonic longitudinal vibration has been applied which was acquired from the USM.

This study was devoted to further improve the processing performance of RUM through a novel mode application of ultrasonic vibration, namely, the longitudinal–torsional composite vibration. Actually, the longitudinal–torsional composite vibration has been successfully applied on other types of ultrasonic vibration-assisted machining as well. For example, Amini et al. investigated the performance of longitudinal–torsional composite vibration in ultrasonic-assisted drilling of the Al 7075-T6 with twist drill, discovering significant reduction of cutting forces compared to the conventional drilling [44]. Asami et al. developed a longitudinal–torsional composite vibration device for the USM of brittle materials with abrasive slurry. Compared to the longitudinal vibration USM [45], the longitudinal–torsional composite vibration was discovered to improve the machining efficiency. Cardoni et al. developed two types of longitudinal–torsional composite vibration-assisted rock sampling devices and verified their corresponding feasibilities [46]. Suzuki et al. utilized a fixed grinding wheel, which was vibrated by a longitudinal–torsional composite vibration, to grind hard ceramics. The experimental results demonstrated that the composite ultrasonic vibration could contribute to the grinding force to be retained low and stable for a long time even without rotating the tool [47]. The successful application of longitudinal–torsional composite vibration on ultrasonic-assisted machining provides promising prospects for the longitudinal–torsional coupled rotary ultrasonic machining (LTC-RUM) of brittle materials.

In this study, feasibility of the LTC-RUM of a brittle material was assessed experimentally by comparison with the conventional rotary ultrasonic longitudinal vibration machining (Con-RUM). Accordingly, the tool for the LTC-RUM was constructed by the addition of helical flutes on the tool of Con-RUM. Consequently, the cutting force, the edge chipping size at the hole exit, and the hole surface roughness were evaluated for the performance comparison between the LTC-RUM and the Con-RUM. Simultaneously, the surface morphology of the blind hole and edge chipping size at the hole entrance were also appraised to contribute to the comparison of material removal mechanism between the LTC-RUM and the Con-RUM.

2 Principle of Longitudinal–Torsional-Coupled Rotary Ultrasonic Machining

In Con-RUM, the longitudinal vibration of the tool for hole drilling is applied; however, in the LTC-RUM, the longitudinal–torsional-coupled vibration of the tool for hole drilling is applied. Figure 2 presents the kinematic view of the LTC-RUM and Con-RUM. Clearly, a coordinate was defined on the tool end face as presented in Fig. 2(a). In LTC-RUM, the moving trajectory of the diamond abrasive can be calculated as follows:

$$\begin{cases} l = A_{\text{tor}} \sin(2\pi ft) + v_s t \\ r = R \\ z = -A_{\text{lon}} \sin(2\pi ft) + f_r t \end{cases} \quad (1)$$

where (l, r, z) is the kinematic position of the abrasive; A_{tor} and A_{lon} are the ultrasonic amplitudes of torsional vibration and longitudinal vibration, respectively; t is the time; f is the ultrasonic frequency; R is the average radius of the tool; f_r is the feedrate of the

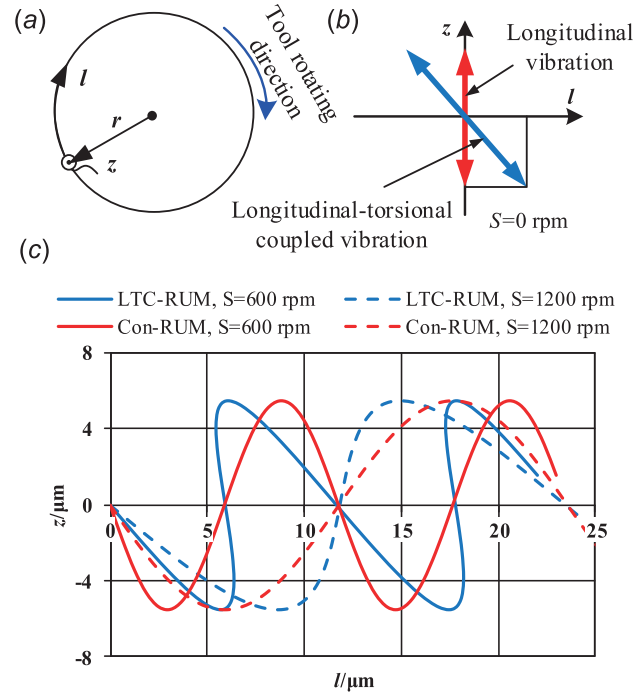


Fig. 2 Kinematic view of LTC-RUM: (a) definition of coordinate, (b) amplitude comparison of LTC-RUM and Con-RUM, and (c) moving trajectory of diamond abrasives

tool; and v_s represents the cutting speed due to tool rotation. The parameter v_s can be calculated by using the following formula:

$$v_s = \frac{2\pi SR}{60} \quad (2)$$

where S is the speed of spindle in rpm.

Figure 2(c) presents the calculated moving trajectory of the diamond abrasive when $R = 3.3$ mm, $A_{\text{lon}} = 5.5$ μm , $A_{\text{tor}} = 3.3$ μm , and $f = 17.60$ kHz. $f_r \gg 2\pi f A_{\text{lon}}$, therefore, v_f is neglected in the previous calculation. Figure 2(c) demonstrates that due to the tool torsional vibration, the moving trajectory of the diamond abrasive in the LTC-RUM was rather different from the moving trajectory in the Con-RUM, in particular, when the spindle speed was relatively low, such as 600 rpm. With the increase in the spindle speed, the cutting speed ratio $2\pi f A_{\text{tor}}/v_s$ becomes significantly lower, resulting in the moving trajectories of the diamond abrasive in both LTC-RUM and Con-RUM tending to be identical. The moving trajectory difference of the diamond abrasive in the LTC-RUM and Con-RUM would highly affect the corresponding processing performances as demonstrated by the experimental results in Sec. 4.

3 Experiment Design

3.1 Experiment Setup. The RUM experiments in this study were performed on an ultrasonic machine tool (Ultrasonic 50, DMG, Stipshausen, Germany). Figure 3 exhibits that the ultrasonic spindle is the key component of the Ultrasonic 50 machine tool. It is equipped with a power supply, a contactless power transmission module, a piezoelectric transducer, an ultrasonic horn, and a diamond core tool. When the experiment was performed, first the power supply converted the 50 Hz current into the AC outputs of ultrasonic frequency. Further, the contactless power transmission module transmitted the ultrasonic-frequency AC signal to the transducer. The transducer consequently converted the AC signal into mechanical vibration. The amplitude of ultrasonic vibration that was produced by the transducer was quite

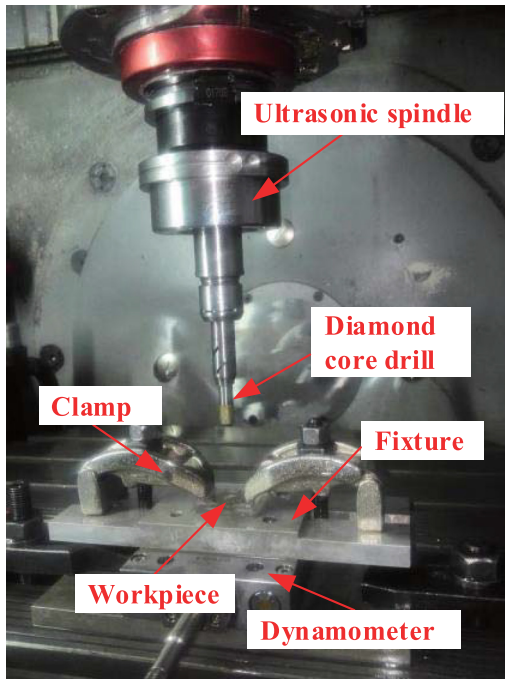


Fig. 3 Experimental setup

low for the machining of brittle materials; therefore, the ultrasonic horn and diamond core tool were well designed to further amplify the ultrasonic amplitude into considerable magnitude. A fixture mounted on a dynamometer was utilized to hold the workpiece with two clamps. The workpiece utilized in this study was a quartz glass of dimension 30 mm × 30 mm × 5 mm. The fixture consists of a hole with diameter of 20 mm and depth of 10 mm underneath the workpiece, which contains the machined cylinder when edge chipping occurs at the hole exit. The corresponding mechanical properties of workpiece are listed in Table 1.

3.2 Accomplishment of Longitudinal–Torsional-Coupled Rotary Ultrasonic Machining by Tool Design. In this study, the LTC vibration was accomplished by an LTC tool that was designed by adding four helical flutes on the diamond core tool of the Con-RUM. The dimensions of the helical flutes are presented in Fig. 4(a). The parameters of the LTC tool were carefully determined based on our design experience of longitudinal–torsional amplifier. For example, the width of helical flutes exhibited insignificant effect on the amplitude ratio of the torsional vibration to the longitudinal vibration. For the determination of width of helical flute, its good machinability is mainly taken into consideration. Moreover, in order to achieve the maximum amplitude ratio of the torsional vibration to the longitudinal vibration, the larger depth of helical flutes is more beneficial. However, these parameters of helical flutes such as the helical angle of 45 deg are not the optimal values. The selection of helical angle of 45 deg was mainly considering the standardized design of mechanical structure.

Table 1 Material properties

Property	Unit	Quartz glass
Young's modulus	GPa	76.7
Vickers hardness	GPa	9.5
Fracture toughness	MPa m ^{1/2}	0.71
Density	g cm ⁻³	2.2
Poisson's ratio	/	0.17

The flutes were cut on to the core drill with the utilization of a five-axes high-speed vertical machining center (DMU60 Mono Block, DMG, Stipshausen, Germany). The cutting method of numerical control multi-axis linkage was used for milling the flutes. A laser fiber vibrometer (LKH008, KEYENCE, Osaka, Japan) with a maximum sampling frequency of 392 kHz and a resolution ratio of 0.1 μm was utilized to measure the ultrasonic amplitude of the Ultrasonic 50, which was mounted by the LTC tool. When the tuning frequency was 17.60 kHz, the ultrasonic amplitude of longitudinal direction reached the corresponding maximum value of 5.5 μm. Consequently, the resonant frequency of Ultrasonic 50 was 17.60 kHz, when the LTC tool was mounted on the machine tool.

In contrast, the ultrasonic amplitude of the torsional direction was difficult to be measured directly by using a laser fiber vibrometer or a capacitive sensor, due to the specific measurement principle. The laser fiber vibrometer is designed to measure the displacement along the laser direction by aiming laser beam at the surface, which is to be measured. Thus, the utilization of laser fiber vibrometer is quite easy and simple to measure the tool longitudinal vibration, which is perpendicular to the tool end face. However, the torsional vibration is parallel to the tool end face, resulting in very difficult and nearly impossible adjustment of laser direction. Similarly, the capacitive probe is designed to measure the displacement whose direction is perpendicular to the probe's work surface. This makes it even more difficult to be used for torsional vibration measurement than laser fiber vibrometer. In this study, the finite elements analysis (FEA) method was utilized for indirect measurement of the ultrasonic amplitude of the torsional direction. The FEA was performed on the harmonic response analysis module of ANSYS. The CAD model utilized for FEA was consistent with the tool utilized in the experiments. Figures 4(b) and 4(c) illustrate the meshing results and loading regime of the FEA method. Figure 4(c) demonstrates that a tuning force was applied on the taper face of the LTC tool. The torsional vibration was accomplished by the longitudinal vibration transformation; therefore, the tuning force direction was set as longitudinal. The material utilized in the FEA was the 45# steel. The corresponding density, elastic module, Poisson's ratio, and damping factor were set at 7.85 g cm⁻³, 210 GPa, 0.27, and 6 × 10⁻⁴, respectively. Figure 4(d) presents the FEA results when the tuning frequency was 17.60 kHz. Figure 4(d) illustrates that a LTC vibration was accomplished at the tool end face. The result regarding the amplitude ratio of torsional vibration to the longitudinal vibration is represented as follows:

$$\frac{A_{\text{tor}}}{A_{\text{lon}}} = 0.49 \quad (3)$$

In general, the actual force applied on the tool taper face should be similar to the tuning force in the simulation. However, direct measurement of that force is extremely difficult. Fortunately, according to mechanical dynamics, the amplitude ratio of torsional vibration to the longitudinal vibration is independent of the tuning force value with the assumption of a linear system. Therefore, though the value of tuning force utilized in the FEA was not the same as the unknown value of actual force acting on the taper face of the tool, the amplitude ratio could be regarded as identical. In contrast, the amplitude ratio ought to have relevance to the frequency of tuning force. Furthermore, the phase difference between the torsional vibration and the longitudinal vibration ought not to be zero, due to the damping effect of the inner friction of material under ultrasonic vibration. Figure 5 exhibits the effect of ultrasonic frequency on the amplitude ratio and phase difference. Figure 5 illustrates that the amplitude ratio varies slightly when the ultrasonic frequency is in the vicinity of 17.60 kHz. Therefore, the simulation error due to the differences in ultrasonic frequency could be regarded as low. Simultaneously, the phase differences between the torsional vibration and the longitudinal vibration were almost zero. Therefore, the phase difference could be neglected and the vibration trajectory of the

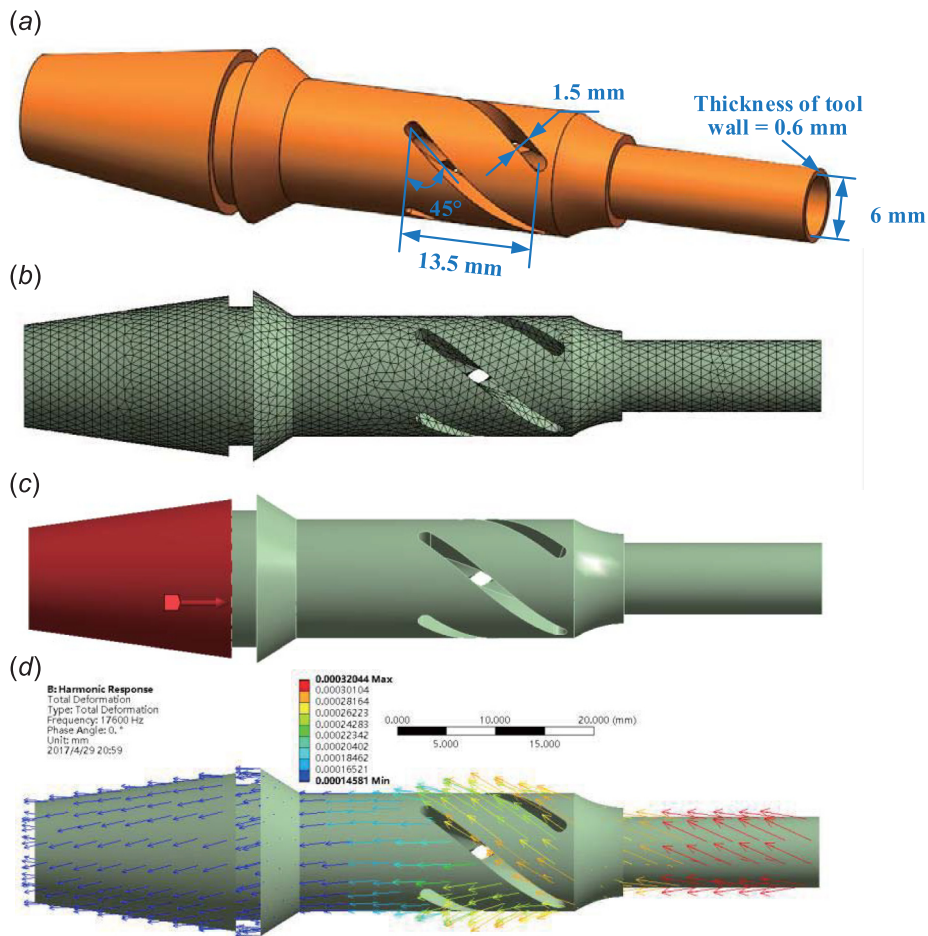


Fig. 4 Tool design: (a) dimension of helical flutes, (b) meshing result of FEA, (c) loading regime of FEA, and (d) simulation result of FEA

diamond abrasive of the LTC tool was regarded as a straight line, as presented in Fig. 2(b).

3.3 Machining Tests. In order to evaluate the processing performance of LTC-RUM and classify the corresponding material removal mechanism, two types of machining experiments were performed. Figure 6 presents that one experiment involves the

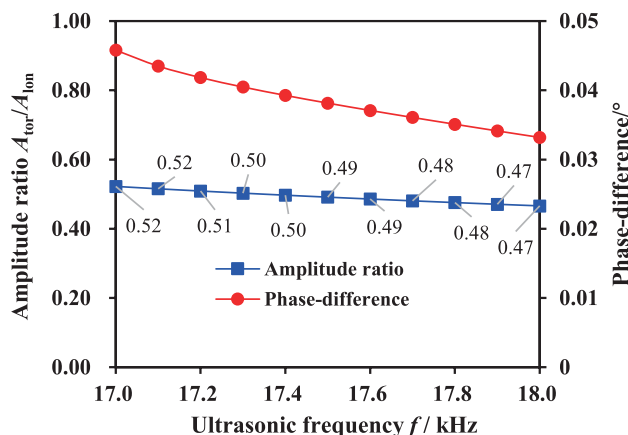


Fig. 5 Effect of ultrasonic frequency on amplitude ratio and phase difference between torsional vibration and longitudinal vibration

drilling of blind holes and the other involves the through holes drilling. Removal of majority of material by RUM was accomplished by the abrasives of the tool; the bottom surfaces of the blind holes were observed by scanning electron microscopy to obtain the material removal characteristic of the LTC-RUM and Con-RUM. In the experiments of drilling through holes, the edge chipping size of the hole edge, the cutting force, and the surface roughness of the hole wall were characterized in order to compare the processing performance between the LTC-RUM and the Con-RUM. Each machining test was repeated two times to reduce the effect of random experiment error. Both the tools utilized for the LTC-RUM and Con-RUM were electroplated with diamond abrasives of the D91 grit. Figure 4(a) shows the tool with the inner diameter of 6 mm and the wall thickness of 0.6 mm.

Tables 2 and 3 list the processing parameters of the blind hole and through hole drilling, respectively. Both the inner and outer coolant lines (Blaser, Switzerland) were utilized during the machining process. Spindle speeds were selected as 600, 1200, and 2400 rpm, respectively, for considering the relative cutting speed ratio $2\pi f A_{tor}/v_s$. For spindle speeds of 600, 1200, and 2400 rpm, the relative cutting speed ratio $2\pi f A_{tor}/v_s$ was <1 , ≈ 1 , and >1 , respectively. Simultaneously, considering the fact that compared to Con-RUM, the feasibility of LTC-RUM was the focus of this study, thus only these three representative values of spindle speed were selected. In further study regarding process optimization, more values would be selected to make variation trend of processing outputs more obvious and reliable.

As presented in Tables 2 and 3, the ultrasonic frequencies of the LTC-RUM and the Con-RUM were slightly different. For the

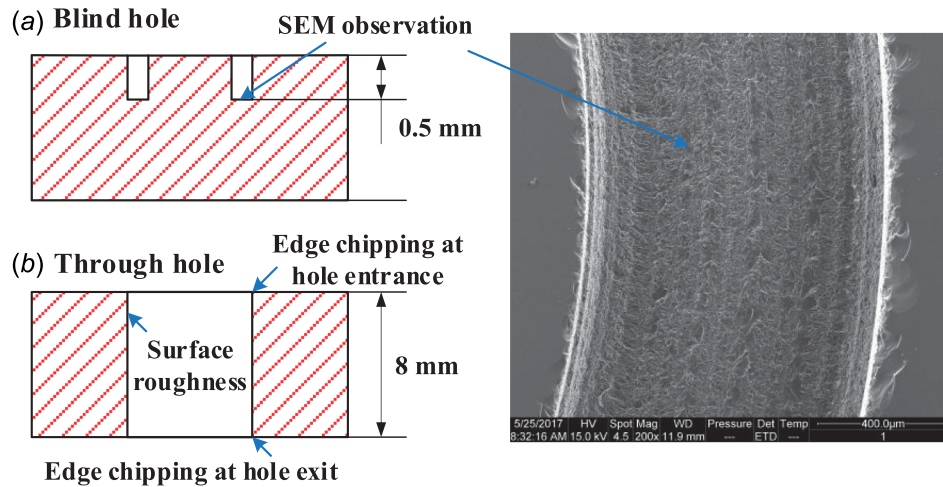


Fig. 6 Two types of experiments: (a) blind hole drilling and (b) through hole drilling

Table 2 Processing parameters of blind hole drilling

Experiment	Spindle speed (rpm)	Feedrate (mm min ⁻¹)	Machining method	Ultrasonic amplitude
Group 1	600, 1200, 2400	2.0	LTC-RUM, $f = 17.60$ kHz	$A_{10n} = 5.5 \mu\text{m}$, $A_{10r}/A_{10n} = 0.49$
Group 2	600, 1200, 2400	2.0	Con-RUM, $f \sim 17.10$ kHz	$A_{10n} = 5\text{--}6 \mu\text{m}$

Table 3 Processing parameters of through hole drilling

Experiment	Spindle speed (rpm)	Feedrate (mm min ⁻¹)	Machining type	Ultrasonic amplitude
Group 3	600, 1200, 2400	1.5, 2.0, 2.5	LTC-RUM, $f = 17.60$ kHz	$A_{10n} = 5.5 \mu\text{m}$, $A_{10r}/A_{10n} = 0.49$
Group 4	600, 1200, 2400	1.5, 2.0, 2.5	Con-RUM, $f \approx 17.10$ kHz	$A_{10n} = 5\text{--}6 \mu\text{m}$

LTC-RUM, the ultrasonic frequency f was 17.60 kHz, which was the resonant frequency of Ultrasonic 50, when it was mounted by LTC tool. For the Con-RUM, the ultrasonic frequency f was 17.10 kHz. The addition of helical flutes was one of the main factors resulting in changes of resonant frequency of machine tools. However, these types of effects are difficult to be characterized analytically. Till date, the finite elements method is still the major method for investigating the abovementioned issues. The relative deviation from 17.60 to 17.10 kHz was below 3%, which could be neglected for the performance comparison of the LTC-RUM and the Con-RUM. Noteworthy, 17.10 kHz was not the resonant frequency of Ultrasonic 50, when it was mounted by the conventional tool for the Con-RUM. The machine tool was tuned at the corresponding resonant frequency, thus the ultrasonic amplitude was as high as $9 \mu\text{m}$. Moreover, the ultrasonic amplitude of Ultrasonic 50 cannot be adjusted freely by the input voltage alteration. According to the authors' previous studies, the ultrasonic power exhibited a positive relationship with the ultrasonic amplitude, whereas the cutting force was found to affect the variation of ultrasonic amplitude [16,48]. Through the ultrasonic power and ultrasonic amplitude measurement of Ultrasonic 50 when the conventional tool for the Con-RUM was utilized, it was discovered that when the tuning frequency was approximately 17.10 kHz, the ultrasonic amplitude was $5\text{--}6 \mu\text{m}$ and the corresponding ultrasonic power was 18–24 W. During the machining process, the ultrasonic power was monitored to guarantee that the ultrasonic amplitude was $5\text{--}6 \mu\text{m}$. Through the application of this aforementioned method, the longitudinal vibration amplitudes of LTC-RUM and Con-RUM were ensured to be almost identical.

3.4 Measurement of Processing Outputs. A piezoelectric dynamometer (9256C2, Kistler Instrument Corp., Switzerland)

was utilized to measure the cutting force during machining. The cutting force signals from the dynamometer were amplified, and consequently, fed to an acquisition card. The recorded data were displayed and processed by using the commercial software DYNOWARE that was provided by Kistler. The sampling frequency of cutting force measurement was set at 100 Hz.

Owing to the ultrasonic vibration of the diamond core drill, the actual cutting force varied with ultrasonic frequency values. The actual cutting force was composed of a direct current component (namely the average cutting force) and the series of the ultrasonic-frequency sinusoid components. In contrast, generally the natural frequency of dynamometer is significantly lower than the ultrasonic frequency. As an example, the natural frequency of the precision Kistler 9256C2 dynamometer was just 4.6 kHz, which would be even lower when the dynamometer was mounted on a workpiece. This resulted in failure in acquiring the ultrasonic-frequency sinusoid component of the actual cutting force regardless of any high sampling frequency. Furthermore, the maximum value of the measured cutting force was relevant to the nature frequency of a certain dynamometer and the applied sampling frequency by a certain investigator. Therefore, considering the corresponding poor agreement among measurement results obtained by different investigators, the maximum value of cutting force measurement was not suitable to be selected as an index for evaluating the processing performance.

In contrast, the information regarding the direct current component of the actual cutting force, namely the average cutting force, is well preserved in the measured cutting force. The measured value of the average cutting force is independent of the natural frequency of the dynamometer and the sampling frequency. As a result, the average cutting force presented good comparability and repeatability. Therefore, in this study, the average cutting force

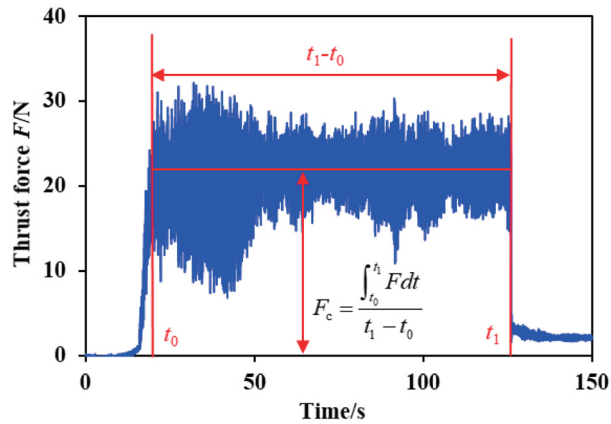


Fig. 7 Calculation of average cutting force F_c

was utilized as an index to compare the processing performance of the LTC-RUM and the Con-RUM. Figure 7 presents a typical curve of the measured cutting force versus time. The average cutting force F_c can be calculated by using the following equation:

$$F_c = \frac{\int_{t_0}^{t_1} F dt}{t_1 - t_0} \quad (4)$$

where F is the time-varying measured cutting force, t_0 and t_1 are the time when the tool begins and completes the drilling of the workpiece, respectively.

The edge chipping size of hole edge is an important index to evaluate the machining-induced damage of RUM. Figure 8 presents a typical edge chipping image of the hole edge. Clearly, D_h is the diameter of machined hole and D_m is the maximum diameter of edge chipping. The edge chipping size d_s can be calculated by using Eq. (5). An optical microscope (55XA, Shanghai Optical Instrument Factory No. 6, Shanghai, China) was utilized to measure the edge chipping size at the hole exit and entrance of each machined hole

$$d_s = \frac{D_m - D_h}{2} \quad (5)$$

The surface morphology of the bottom of the blind hole was characterized by using a scanning electron microscope (QUANTA 200 FEG, FEI, Hillsboro, OR). A surface roughness tester (Surtronic 25, Taylor Hobson, Britain) was utilized to measure the roughness R_a of the hole wall. Figure 9 exhibits four different positions of the hole wall to measure the roughness. The average

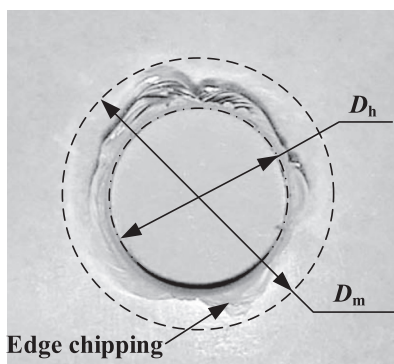


Fig. 8 Representation of edge chipping size

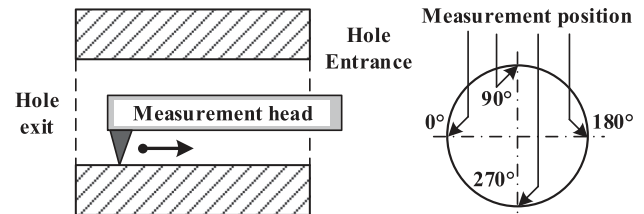


Fig. 9 Method for the measurement of roughness of hole surface

value of four measurements was utilized to evaluate the surface quality of the hole wall.

4 Results and Discussion

4.1 Edge Chipping at Hole Entrance.

Figure 10 presents the edge chipping size results at hole entrance. Figure 10 shows that the edge chipping sizes at the hole entrance in LTC-RUM are greater than the edge chipping sizes in Con-RUM. Moreover, within the two major processing parameters, namely the spindle speed and feedrate, the spindle speed exhibited significant effect on the edge chipping size at the hole entrance. The edge chipping size at the hole entrance increased with the increase in the spindle speed regardless of machining methods. In general, the edge chipping size at the hole entrance in brittle material drilling is significantly lower than that at the hole exit. Though the edge chipping is not the major machining-induced defect of RUM, it can assist researchers to demonstrate the material removal mechanism involved in the RUM of brittle materials.

Lv et al. [49] reported that the edge chipping at the hole entrance was induced directly by the removal of material by RUM. Figure 11(a) demonstrates that in the RUM of brittle materials, radial cracks and lateral cracks are produced due to the indentation of the diamond abrasive on the workpiece material. Figure 11(b) clearly shows that the lateral cracks produced by different abrasives propagate and interact with each other, resulting in the material removal. Simultaneously, Fig. 11(c) presents that at the hole entrance edge, certain lateral cracks propagate to the material surface, consequently inducing serrated edge chipping. The edge chipping size at the hole entrance exhibited positive relevance to the lateral crack length. In other words, a higher edge chipping size at the hole entrance was accompanied with higher length of the lateral crack [49]. Therefore, the higher edge chipping size at the hole entrance of LTC-RUM compared to the edge

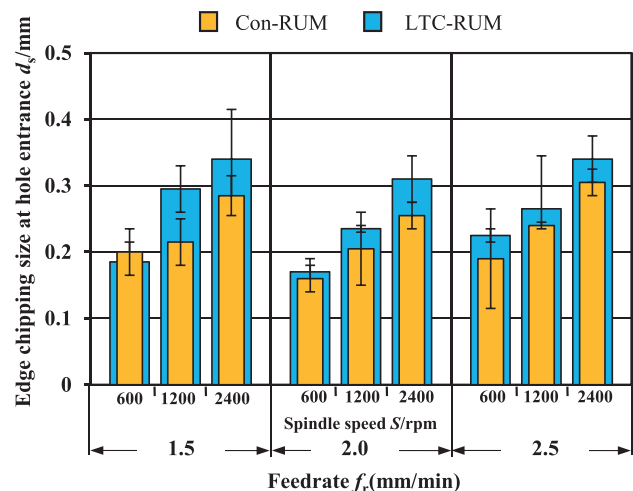


Fig. 10 Effect of processing parameters on edge chipping size at hole entrance

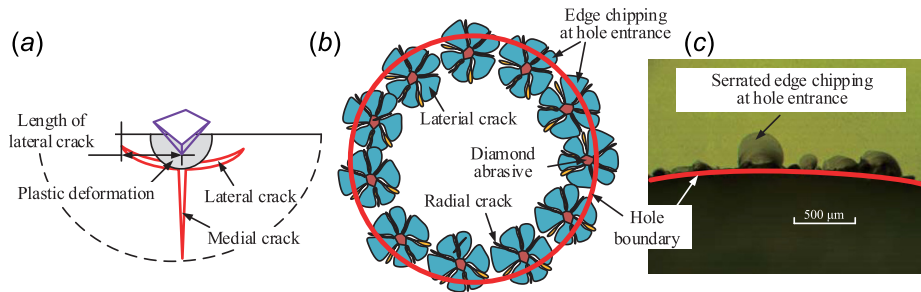


Fig. 11 Edge chipping at hole entrance: (a) crack system produced by diamond abrasives indentation on workpiece material, (b) formation mechanism of edge chipping at hole entrance [49], and (c) serrated morphology of edge chipping at hole entrance

Table 4 Bottom surface morphology of blind holes

Machining method	$S = 600$ rpm	$S = 1200$ rpm	$S = 2400$ rpm
LTC-RUM			
Con-RUM			

chipping size of the Con-RUM indicated that the lengths of lateral cracks produced in LTC-RUM were greater than the lengths of lateral cracks produced in Con-RUM.

Furthermore, Lv et al. [49] conducted conventional grinding and Con-RUM to drill holes in brittle materials. It was discovered that the edge chipping size at the hole entrance in both the conventional grinding and the Con-RUM increased with the increase in the spindle speed, which indicated the increase in the lengths of lateral cracks with the increase in the cutting speed. Moreover, it was discovered that the maximum cutting speed of the diamond abrasive in Con-RUM exceeded the maximum cutting speed in conventional grinding due to the tool longitudinal vibration; therefore, the edge chipping size at the hole entrance in Con-RUM exceeded the edge chipping size in conventional grinding. Similarly, in this study, due to the existence of torsional vibration in LTC-RUM, the maximum cutting speed of the diamond abrasive in LTC-RUM exceeded the maximum cutting speed in Con-RUM. Therefore, the edge chipping size of the LTC-RUM was higher than the edge chipping size of Con-RUM. Simultaneously, the edge chipping size of the LTC-RUM increased with the increase in the spindle speed, due to the increase in the maximum cutting speed of the diamond abrasive.

The diameter of machined holes is also an important indicator of hole machining. Considering that the hole diameter is mainly determined by the outer diameter of diamond core drill, the diameter of machined hole was not paid attention to in this study. However, the tolerance of hole diameter would be affected by the material removal process related to lateral cracks. In some

applications demanding high-precision, the effect of processing parameters and its mechanism on the tolerance of hole diameter are required to be clarified, for example, how the hole diameter is affected by the lateral cracks with the increase in the spindle speed requires further explorations.

4.2 Material Removal Characteristic From Blind Hole Observation. Table 4 summarizes the bottom surface morphologies of the blind hole. Surface morphologies clearly exhibit the existence of distinct shell-like craters. The craters are the remaining traces of material removal induced by the propagation of lateral cracks. The sizes of the craters indicated the lengths of lateral cracks. Apparent differences in surface morphologies between the LTC-RUM and the Con-RUM could be clearly observed. The sizes of the craters in the surface morphologies of LTC-RUM were higher than crater sizes of Con-RUM, indicating that the lengths of lateral cracks of the LTC-RUM were higher than those of the Con-RUM. This conclusion is consistent with the conclusion obtained from the edge chipping size analysis at the hole entrance.

Though the LTC-RUM could not reduce the edge chipping defect size at the hole entrance compared to the Con-RUM, the higher length of the lateral cracks in LTC-RUM would be beneficial for the high efficiency material removal. This was further discussed in the section regarding the cutting force.

4.3 Cutting Force. Figure 12 presents the comparison of cutting forces between the LTC-RUM and the Con-RUM. Figure 12

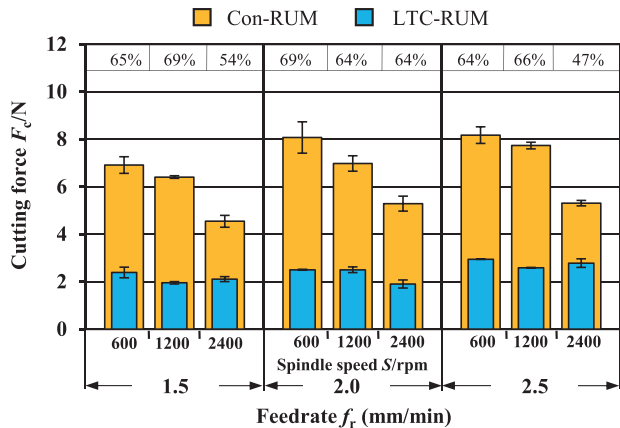


Fig. 12 Effect of processing parameters on cutting force

shows that the LTC-RUM can significantly reduce the cutting force compared to the Con-RUM. The cutting force reduction ratio of the LTC-RUM to Con-RUM is presented at the top of Fig. 12. It was observed that the LTC-RUM could reduce the cutting force by 47–69%. The calculation results revealed that the average cutting force reduction ratio was 55%. The minimum ratios of cutting force reduction under certain feedrate were obtained at the highest spindle speed. It is well known that the Con-RUM can reduce the cutting force by approximately 50% compared to conventional grinding, consequently resulting in superior processing quality, such as the improved hole exit quality and the extended tool life [18,30]. Furthermore, the results of authors' previous studies [16,48] indicated that the cutting force exhibited bad effects on the stability of ultrasonic vibration during the machining process, consequently limiting the further improvement in the efficiency of the RUM. Therefore, significant reduction in cutting force of LTC-RUM was beneficial not only for the improvement in the processing quality of RUM, but also for the stability of ultrasonic vibration. The reduction was beneficial for the machining efficiency.

Furthermore, Fig. 12 presents that the increase in the feedrate leads to the increase in the cutting force, whereas it decreases as the spindle speed increases in Con-RUM. In contrast, though the cutting force increases with the increase in the feedrate, the other processing parameter, namely the spindle speed, does not have

apparent effect on the cutting force variation in LTC-RUM. In general, in hole drilling, the spindle speed is regarded as a dominant factor that affects the cutting force such as the results of Con-RUM. The unapparent dependency of cutting force on the spindle speed in LTC-RUM should be attributed to the corresponding material removal mechanism. In terms of material removal mechanism, the differences in abrasive moving trajectory between the LTC-RUM and the Con-RUM ought to be responsible.

Figure 13 illustrates the calculations performed for cutting force. These calculations were utilized to discuss the cause of reduction in cutting force of the LTC-RUM. Figure 13(a) presents that in Con-RUM, the diamond abrasives were in contact with and separated from the workpiece material periodically, with an indentation depth of δ_{Con} in an ultrasonic frequency. The contact duration Δt_{Con} in one vibration period can be calculated as follows:

$$\Delta t_{Con} = \frac{1}{\pi f} \arccos\left(1 - \frac{\delta_{Con}}{A_{lon}}\right) \quad (6)$$

Through

$$\arccos(1 - \delta_{Con}/A_{lon}) \approx \sqrt{2\delta_{Con}/A_{lon}} \quad (7)$$

Equation (6) can be simplified as

$$\Delta t_{Con} \approx \frac{\sqrt{2}}{\pi f} \left(\frac{\delta_{Con}}{A_{lon}}\right)^{\frac{1}{2}} \quad (8)$$

Jiao [50] made an assumption that all effective diamond abrasives that participated in the material removal indented the workpiece material with the same depth, thus the impact force acting on the workpiece material can be calculated as follows:

$$F_{m,Con} = \frac{1}{2} m \xi \delta_{Con}^2 \tan^2 \psi H_v \quad (9)$$

where ξ is the geometrical factor of the indenter, ψ is the semivertical angle of the indenter, H_v is the microhardness of the workpiece material, and m is the number of effective diamond particles. Through a triple wave utilization to simplify the actual cutting force in one vibration period, the average cutting force $F_{c,Con}$ can be derived as represented below:

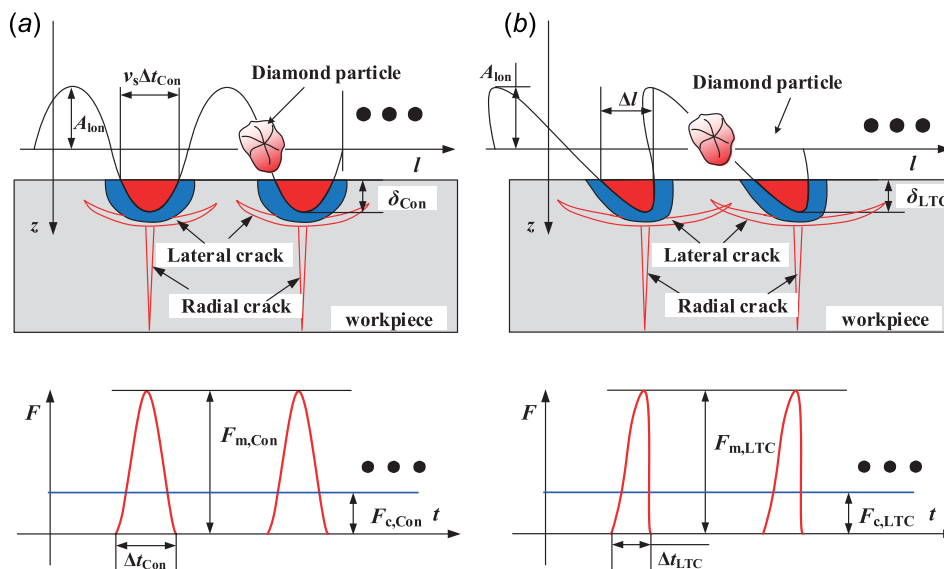


Fig. 13 Analysis of cutting force calculation: (a) Con-RUM and (b) LTC-RUM

$$\frac{F_{c,Con}}{f} = \frac{F_{m,Con}\Delta t}{2} \quad (10)$$

Through substitution of Eqs. (8) and (9) into Eq. (10), the cutting force $F_{c,Con}$ can be calculated as follows:

$$F_{c,Con} = \frac{\sqrt{2}m\zeta \tan^2\psi H_v}{4\pi\sqrt{A_{lon}}} \cdot \delta_{Con}^{\frac{5}{2}} \quad (11)$$

Similarly, as presented in Fig. 13(b), in LTC-RUM, the contact duration Δt_{LTC} of the diamond abrasive on the workpiece material in one vibration period can be calculated by

$$\Delta t_{LTC} = \frac{\lambda}{\pi f} \arccos\left(1 - \frac{\delta_{Con}}{A_{lon}}\right) \quad (12)$$

where δ_{LTC} is the indentation depth of diamond abrasive on the workpiece material in LTC-RUM and λ is a proportionality coefficient that characterizes the unloading effect when the diamond abrasive is pulled out from the workpiece material. Figure 13 shows that the pull out processes of the diamond abrasive in the Con-RUM and the LTC-RUM are rather different. In Con-RUM, when the diamond abrasive was pulled out from the workpiece material, it continued to move horizontally and scratched the material. Consequently, as long as the diamond abrasive did not leave the workpiece surface, it acted as a force on the material. In contrast, due to the torsional vibration in LTC-RUM, when the diamond abrasive was pulled out from the workpiece material (namely the unloading process), it moved nearly vertically. Owing to the existence of plastic deformation and propagation of the lateral cracks, the unloading process was faster than the loading process. Therefore, λ ought to comply with $0.5 < \lambda < 1$.

Consequently, in reference to the modeling process of cutting force $F_{c,Con}$, the cutting force $F_{c,LTC}$ in LTC-RUM can be calculated as follows:

$$F_{c,LTC} = \lambda \cdot \frac{\sqrt{2}m\zeta \tan^2\psi H_v}{4\pi\sqrt{A_{lon}}} \cdot \delta_{LTC}^{\frac{5}{2}} \quad (13)$$

Equations (11) and (13) establish the dependency of cutting force on the indentation depth in the Con-RUM and LTC-RUM, respectively. These equations contribute to the further discussion of the cutting force variation tendency, as presented in Fig. 13(a). Two major phenomena should be explained. One is the cutting force reduction of LTC-RUM compared to the Con-RUM. The other is the unapparent dependency of cutting force on the spindle speed in LTC-RUM.

First, from Eqs. (11) and (13), the following equation can be obtained:

$$\frac{F_{c,LTC}}{F_{c,Con}} = \lambda \cdot \left(\frac{\delta_{LTC}}{\delta_{Con}}\right)^{\frac{5}{2}} \quad (14)$$

Cong et al. [27] reported that the indentation depth of the abrasive was relative to the lateral crack length. A higher length of lateral crack was accompanied with a lower indentation depth [27]. According to the results mentioned in Secs. 4.1 and 4.2, the abrasive indentation depth in LTC-RUM was higher than that in Con-RUM. It could also be derived that the lateral crack length in LTC-RUM was lower than the lateral crack length in Con-RUM, i.e., $\delta_{LTC}/\delta_{Con} < 1$. Therefore, based on Eq. (14), the LTC-RUM could reduce the cutting force compared to the Con-RUM.

Second, Cong et al. [27] further reported that the indentation depth of the abrasive increased with the increase in the feedrate; however, it decreased with the increase in the spindle speed to guarantee that the micromaterial removal rate was equal to the macromaterial removal due to the tool feed. Therefore, in LTC-RUM, δ_{LTC} ought to increase as the feedrate increased, whereas it

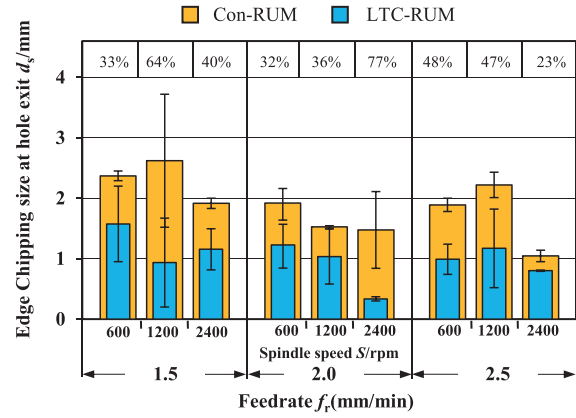


Fig. 14 Comparison of edge chipping sizes at hole exit

decreased as the spindle speed increased. In contrast, as presented in Fig. 2, the differences in the moving trajectory of the diamond abrasive between the LTC-RUM and the Con-RUM decreased with the increase in the spindle speed. This resulted in increase in the value of λ with the increase in the spindle speed. According to Eq. (13), the adverse variation tendency of δ_{LTC} and λ resulted in the unapparent dependency of cutting force on the spindle speed, as presented in Fig. 12. Furthermore, according to the aforementioned analysis, the cutting force in LTC-RUM would increase as the feedrate increased due to the increase in δ_{LTC} . The results presented in Fig. 12 verified this induction.

4.4 Edge Chipping at Hole Exit.

The edge chipping at the hole exit is the most severe machining induced defect in the RUM of brittle materials, which affects the productivity as well as the design ability of products, produced from brittle materials [39]. Figure 14 presents the comparison of edge chipping sizes at the hole exit between the LTC-RUM and the Con-RUM. Figure 14 exhibits that the LTC-RUM could significantly reduce the edge chipping size at the hole exit compared to the Con-RUM. The edge reduction size ratio of LTC-RUM to Con-RUM is presented at the top of Fig. 14. Clearly, the LTC-RUM could reduce the cutting force by 23–77%. Through calculation, the average edge chipping size reduction ratio was found to be 45%.

According to the authors' previous study [35], the edge chipping formation at the hole exit could be attributed to the propagation of machining-induced subsurface cracks (namely the radial cracks) under the driving force (namely the impact force F_m as presented in Fig. 13(a)). In order to discuss the edge chipping reduction mechanism of the LTC-RUM compared to the Con-RUM, the sizes of machining-induced radial cracks and the impact force should be analyzed. A higher size of radial cracks and higher impact force resulted in higher edge chipping size at the hole exit. Marshall and Abdalla [51] demonstrated that the size of radial cracks was positively dependent on the impact force F_m . Furthermore, the impact force was found to be positively dependent on the indentation depth [50]. Therefore, a higher indentation depth would result in higher edge chipping size at the hole exit. As demonstrated in Sec. 4.4, the indentation depth of LTC-RUM was lower than the indentation depth of Con-RUM, consequently inducing the edge chipping reduction of the LTC-RUM compared to the Con-RUM.

4.5 Hole Surface Roughness. Figure 15 presents the comparison of surface roughness values of the hole wall. Figure 15 presents that the LTC-RUM could improve the hole surface quality through reduction in the surface roughness. Moreover, the spindle speed was the main factor affecting the surface roughness. Figure 15 clearly shows that the spindle speed significantly affects

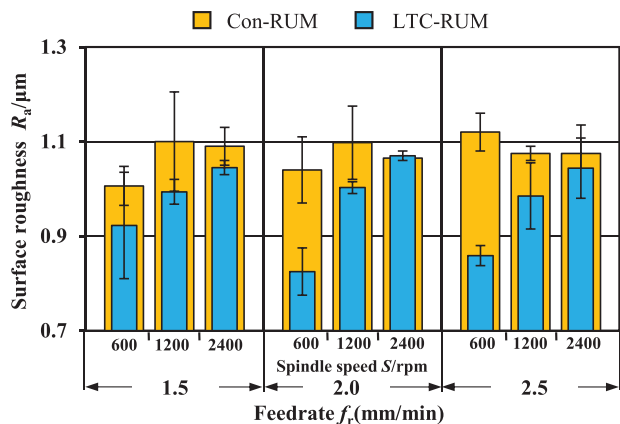


Fig. 15 Comparison of surface roughness of hole wall

the surface roughness of the hole wall in LTC-RUM. The surface roughness of the hole wall in LTC-RUM increased as the spindle speed increased. In contrast, the surface roughness in Con-RUM varied in an unapparent manner with the increase in the spindle speed in Con-RUM. In general, the surface roughness of hole wall in conventional diamond drilling of brittle material decreases with the increasing spindle speed due to the decreasing feed per revolution of tool. However, in Con-RUM, the effect of spindle speed on the surface roughness of hole wall would be complicated. On the one hand, the increase of spindle speed would reduce the feed per revolution of tool, which would be beneficial for the hole wall finishing. On the other hand, the increase of spindle speed would weaken the superiority of ultrasonic machining by smoothing the moving trajectory of diamond abrasive. However, in LTC-RUM, it is believed that the decrease in the surface roughness would be attributed to the two-dimensional ultrasonic vibration, namely the longitudinal-torsional vibration. The superior effect of two-dimensional ultrasonic vibration would be suppressed gradually with the increasing spindle speed as shown in Fig. 2.

The different varying tendency of surface roughness with the increasing spindle speed in LTC-RUM and Con-RUM resulted in that the extent of reduction of surface roughness of the LTC-RUM compared to the Con-RUM decreased as the spindle speed increased. Compared to the Con-RUM, the LTC-RUM can work under a relatively low spindle speed with low surface roughness and low cutting force, thus proving to be beneficial for the tool life extension.

Though the majority of material removal in RUM is accomplished by the diamond abrasives of the tool end face, the surface generation of the hole wall is accomplished by the diamond abrasives of the tool wall face [52]. Wang et al. indicated that the moving trajectory of the diamond abrasives highly affected the machined surface smoothing. As illustrated in Sec. 2, the spindle speed significantly affected the moving trajectory of the diamond abrasive in LTC-RUM, whereas the moving trajectory deviation between the LTC-RUM and the Con-RUM decreased as the spindle speed increased. This was the reason responsible for the surface roughness distinction between the LTC-RUM and the Con-RUM as the spindle speed increased. Figure 15 presents that when the spindle speed was as high as 2400 rpm, the distinctions of surface roughness between the LTC-RUM and the Con-RUM were already rather low.

5 Conclusions

An experimental study on quartz glass was conducted to investigate the feasibility of LTC-RUM of a brittle material through comparison with the Con-RUM. The LTC-RUM was accomplished through the addition of helical flutes on the Con-RUM tool. The ultrasonic amplitudes of longitudinal vibration in both the LTC-RUM and the Con-RUM were retained identical. The

processing performance, such as the edge chipping defect at the hole entrance and exit, the cutting force, and the surface roughness of the hole wall were also evaluated. Moreover, the bottom surface morphologies were observed to contribute to the material removal characteristic observation of the LTC-RUM. Based on the findings, the following conclusions were drawn:

- (1) The edge chipping defect at the hole entrance was produced during material removal, which resulted from the propagation of lateral cracks when the diamond abrasive impacted the workpiece surface. The edge chipping size at the hole entrance of LTC-RUM was higher than the edge chipping size of Con-RUM, indicating that the lengths of lateral cracks in LTC-RUM were greater than the lengths of lateral cracks in Con-RUM, due to the maximum increase in the cutting speed. The morphological results obtained for the bottom surface of the blind holes were in good agreement with the aforementioned induction. The sizes of the craters in the surface morphologies of LTC-RUM were greater than that the crater sizes of Con-RUM.
- (2) Owing to the faster unloading process that resulted from the specific moving trajectory of the diamond abrasives and the higher length of lateral cracks in LTC-RUM, the LTC-RUM could reduce the cutting force by 55% on an average compared to the Con-RUM. Both cutting forces of LTC-RUM and Con-RUM increased as the federate increased. In contrast, because the spindle speed would affect the moving trajectory and the indentation depth of diamond abrasives, it did not significantly affect the variation of cutting force in LTC-RUM. However, the cutting force decreased as the spindle speed increased in Con-RUM.
- (3) Attributed to the lower indentation depth of the diamond abrasive in LTC-RUM resulting from the higher lengths of lateral cracks, the LTC-RUM could reduce the edge chipping size at the hole exit by 45% on an average compared to the Con-RUM.
- (4) The LTC-RUM could also improve the hole quality through reduction in the surface roughness under relatively low spindle speed compared to the Con-RUM. The spindle speed significantly affected the moving trajectory of the diamond abrasive in LTC-RUM and the deviation of moving trajectory between the LTC-RUM and the Con-RUM decreased as the spindle speed increased; therefore, the reduction ratio of surface roughness of the LTC-RUM compared to Con-RUM decreased as the spindle speed increased.

Funding Data

- National Natural Science Foundation of China (Grant No. 51475260).
- Natural Science Foundation of Beijing Municipality (Grant No. 3141001).

References

- [1] Arif, M., Xinquan, Z., Rahman, M., and Kumar, S., 2013, "A Predictive Model of the Critical Undeformed Chip Thickness for Ductile—Brittle Transition in Nano-Machining of Brittle Materials," *Int. J. Mach. Tools Manuf.*, **64**, pp. 114–122.
- [2] Chen, J., Fang, Q., and Li, P., 2015, "Effect of Grinding Wheel Spindle Vibration on Surface Roughness and Subsurface Damage in Brittle Material Grinding," *Int. J. Mach. Tools Manuf.*, **91**, pp. 12–23.
- [3] Malkin, S., and Hwang, T. W., 1996, "Grinding Mechanisms for Ceramics," *CIRP Ann. Manuf. Technol.*, **45**(2), pp. 569–580.
- [4] Nicholls, C. J., Boswell, B., Davies, I. J., and Islam, M. N., 2017, "Review of Machining Metal Matrix Composites," *Int. J. Adv. Manuf. Technol.*, **90**(9–12), pp. 2429–2441.
- [5] Pei, Z. J., Fisher, G. R., and Liu, J., 2008, "Grinding of Silicon Wafers: A Review From Historical Perspectives," *Int. J. Mach. Tools Manuf.*, **48**(12–13), pp. 1297–1307.
- [6] Zhang, L., Ren, C., Ji, C., Wang, Z., and Chen, G., 2016, "Effect of Fiber Orientations on Surface Grinding Process of Unidirectional C/SiC Composites," *Appl. Surf. Sci.*, **366**, pp. 424–431.

- [7] Li, H., Lin, B., Wan, S., Wang, Y., and Zhang, X., 2016, "An Experimental Investigation on Ultrasonic Vibration Assisted Grinding of SiO₂/SiO₂ Composites," *Mater. Manuf. Processes*, **31**(7), pp. 887–895.
- [8] Li, W., Zhang, R., Liu, Y., Wang, C., Wang, J., Yang, X., and Cheng, L., 2016, "Effect of Different Parameters on Machining of SiC/SiC Composites Via Pico-Second Laser," *Appl. Surf. Sci.*, **364**, pp. 378–387.
- [9] Samant, A. N., and Dahotre, N. B., 2009, "Laser Machining of Structural Ceramics—A Review," *J. Eur. Ceram. Soc.*, **29**(6), pp. 969–993.
- [10] Wei, C., Zhao, L., Hu, D., and Ni, J., 2013, "Electrical Discharge Machining of Ceramic Matrix Composites With Ceramic Fiber Reinforcements," *Int. J. Adv. Manuf. Technol.*, **64**(1–4), pp. 187–194.
- [11] Kohorst, P., Tegtmeyer, S., Biskup, C., and Bach, F. W., 2014, "Machining Human Dentin by Abrasive Water Jet Drilling," *Biomed. Mater. Eng.*, **24**(2), pp. 1485–1495.
- [12] Das, S., Kumar, S., Doloi, B., and Bhattacharyya, B., 2016, "Experimental Studies of Ultrasonic Machining on Hydroxyapatite Bio-Ceramics," *Int. J. Adv. Manuf. Technol.*, **86**(1–4), pp. 829–839.
- [13] Thoe, T. B., Aspinwall, D. K., and Wise, M. L. H., 1998, "Review on Ultrasonic Machining," *Int. J. Mach. Tools Manuf.*, **38**(4), pp. 239–255.
- [14] Ahluwalia, D., Borrelli, M. J., Smithson, K., Rajurkar, K. P., and Malshe, A. P., 2014, "Ultrasonic Machining of Biomass Using Biodegradable Slurry," *CIRP Ann.-Manuf. Technol.*, **63**(1), pp. 217–220.
- [15] Singh, R. P., and Singhal, S., 2016, "Rotary Ultrasonic Machining: A Review," *Mater. Manuf. Processes*, **31**(14), pp. 1795–1824.
- [16] Wang, J., Feng, P., Zhang, J., Cai, W., and Shen, H., 2017, "Investigations on the Critical Feed Rate Guaranteeing the Effectiveness of Rotary Ultrasonic Machining," *Ultrasonics*, **74**, pp. 81–88.
- [17] Ning, F. D., Cong, W. L., Pei, Z. J., and Treadwell, C., 2016, "Rotary Ultrasonic Machining of CFRP: A Comparison With Grinding," *Ultrasonics*, **66**, pp. 125–132.
- [18] Feng, P., Wang, J., Zhang, J., and Zheng, J., 2017, "Drilling Induced Tearing Defects in Rotary Ultrasonic Machining of C/SiC Composites," *Ceram. Int.*, **43**(1, Pt. A), pp. 791–799.
- [19] Feng, P., Liang, G., and Zhang, J., 2014, "Ultrasonic Vibration-Assisted Scratch Characteristics of Silicon Carbide-Reinforced Aluminum Matrix Composites," *Ceram. Int.*, **40**(7), pp. 10817–10823.
- [20] Cao, J., Wu, Y., Lu, D., Fujimoto, M., and Nomura, M., 2014, "Material Removal Behavior in Ultrasonic-Assisted Scratching of SiC Ceramics With a Single Diamond Tool," *Int. J. Mach. Tools Manuf.*, **79**, pp. 49–61.
- [21] Zhang, C., Feng, P., and Zhang, J., 2013, "Ultrasonic Vibration-Assisted Scratch-Induced Characteristics of C-Plane Sapphire With a Spherical Indenter," *Int. J. Mach. Tools Manuf.*, **64**, pp. 38–48.
- [22] Singh, R. P., and Singhal, S., 2016, "Investigation of Machining Characteristics in Rotary Ultrasonic Machining of Alumina Ceramic," *Mater. Manuf. Processes*, **32**(3), pp. 309–326.
- [23] Gupta, V., and Pandey, P. M., 2016, "An In-Vitro Study of Cutting Force and Torque During Rotary Ultrasonic Bone Drilling," *Proc. Inst. Mech. Eng., Part B*, epub.
- [24] Jain, A. K., and Pandey, P. M., 2016, "Study of Peck Drilling of Borosilicate Glass With μ RUM Process for MEMS," *J. Manuf. Processes*, **22**, pp. 134–150.
- [25] Zhang, C. L., Feng, P. F., Pei, Z. J., and Cong, W. L., 2013, "Rotary Ultrasonic Machining of Sapphire: Feasibility Study and Designed Experiments," *Key Eng. Mater.*, **589–590**, pp. 523–528.
- [26] Gupta, V., and Pandey, P. M., 2016, "Experimental Investigation and Statistical Modeling of Temperature Rise in Rotary Ultrasonic Bone Drilling," *Med. Eng. Phys.*, **38**(11), pp. 1330–1338.
- [27] Cong, W. L., Pei, Z. J., Sun, X., and Zhang, C. L., 2014, "Rotary Ultrasonic Machining of CFRP: A Mechanistic Predictive Model for Cutting Force," *Ultrasonics*, **54**(2), pp. 663–675.
- [28] Xiao, X., Zheng, K., and Liao, W., 2014, "Theoretical Model for Cutting Force in Rotary Ultrasonic Milling of Dental Zirconia Ceramics," *Int. J. Adv. Manuf. Technol.*, **75**(9–12), pp. 1263–1277.
- [29] Liu, D., Cong, W. L., Pei, Z. J., and Tang, Y., 2012, "A Cutting Force Model for Rotary Ultrasonic Machining of Brittle Materials," *Int. J. Mach. Tools Manuf.*, **52**(1), pp. 77–84.
- [30] Wang, J., Feng, P., Zhang, J., Zhang, C., and Pei, Z., 2016, "Modeling the Dependency of Edge Chipping Size on the Material Properties and Cutting Force for Rotary Ultrasonic Drilling of Brittle Materials," *Int. J. Mach. Tools Manuf.*, **101**, pp. 18–27.
- [31] Anil Kumar, P. M. P., and Jain, A., 2017, "Modelling of Un-Deformed Chip Thickness in RUM Process and Study of Size Effects in μ -RUM," *Ultrasonics*, **77**, 1–16.
- [32] Yuan, S., Zhang, C., Amin, M., Fan, H., and Liu, M., 2015, "Development of a Cutting Force Prediction Model Based on Brittle Fracture for Carbon Fiber Reinforced Polymers for Rotary Ultrasonic Drilling," *Int. J. Adv. Manuf. Technol.*, **81**(5–8), pp. 1223–1231.
- [33] Pei, Z. J., and Ferreira, P. M., 1998, "Modeling of Ductile-Mode Material Removal in Rotary Ultrasonic Machining," *Int. J. Mach. Tools Manuf.*, **38**(10–11), pp. 1399–1418.
- [34] Pei, Z. J., Prabhakar, D., Ferreira, P. M., and Haselkorn, M., 1995, "A Mechanistic Approach to the Prediction of Material Removal Rates in Rotary Ultrasonic Machining," *ASME J. Eng. Ind.*, **117**(2), pp. 142–151.
- [35] Wang, J., Zha, H., Feng, P., and Zhang, J., 2016, "On the Mechanism of Edge Chipping Reduction in Rotary Ultrasonic Drilling: A Novel Experimental Method," *Precis. Eng.*, **44**, pp. 231–235.
- [36] Lv, D., Huang, Y., Tang, Y., and Wang, H., 2013, "Relationship Between Subsurface Damage and Surface Roughness of Glass BK7 in Rotary Ultrasonic Machining and Conventional Grinding Processes," *Int. J. Adv. Manuf. Technol.*, **67**(1–4), pp. 613–622.
- [37] Liu, J. W., Baek, D. K., and Ko, T. J., 2014, "Chipping Minimization in Drilling Ceramic Materials With Rotary Ultrasonic Machining," *Int. J. Adv. Manuf. Technol.*, **72**(9–12), pp. 1527–1535.
- [38] Li, Z. C., Cai, L., Pei, Z. J., and Treadwell, C., 2006, "Edge-Chipping Reduction in Rotary Ultrasonic Machining of Ceramics: Finite Element Analysis and Experimental Verification," *Int. J. Mach. Tools Manuf.*, **46**(12–13), pp. 1469–1477.
- [39] Wang, J., Feng, P., and Zhang, J., 2016, "Reduction of Edge Chipping in Rotary Ultrasonic Machining by Using Step Drill: A Feasibility Study," *Int. J. Adv. Manuf. Technol.*, **87**(9–12), pp. 2809–2819.
- [40] Wang, J., Zhang, J., Feng, P., Zheng, J., and Zhang, J., 2016, "Improving Hole Exit Quality in Rotary Ultrasonic Machining of Ceramic Matrix Composites Using a Compound Step-Taper Drill," *Ceram. Int.*, **42**(12), pp. 13387–13394.
- [41] Wang, J., Feng, P., and Zhang, J., 2016, "Investigations on the Edge-Chipping Reduction in Rotary Ultrasonic Machining Using a Conical Drill," *Proc. Inst. Mech. Eng., Part B*, **230**(7), pp. 1254–1263.
- [42] Cong, W. L., Pei, Z. J., Deines, T. W., and Treadwell, C., 2011, "Rotary Ultrasonic Machining of CFRP Using Cold Air as Coolant: Feasible Regions," *J. Reinf. Plast. Compos.*, **30**(10), pp. 899–906.
- [43] Liu, J., Zhang, D., Qin, L., and Yan, L., 2012, "Feasibility Study of the Rotary Ultrasonic Elliptical Machining of Carbon Fiber Reinforced Plastics (CFRP)," *Int. J. Mach. Tools Manuf.*, **53**(1), pp. 141–150.
- [44] Amini, S., Soleimani, M., Pakinat, H., and Lotfi, M., 2017, "Effect of Longitudinal-Torsional Vibration in Ultrasonic-Assisted Drilling," *Mater. Manuf. Processes*, **32**(6), pp. 616–622.
- [45] Asami, T., and Miura, H., 2015, "Study of Ultrasonic Machining Using Longitudinal and Torsional Vibration," IEEE International Ultrasonics Symposium (IUS), Taipei, Taiwan, Oct. 21–24, pp. 1–4.
- [46] Cardoni, A., Harkness, P., and Lucas, M., 2010, "Ultrasonic Rock Sampling Using Longitudinal-Torsional Vibrations," *Phys. Proc.*, **3**(1), pp. 125–134.
- [47] Suzuki, K., Tochmai, H., Uematsu, T., Mishiro, S., and Nakagawa, T., 1993, "A New Grinding Method for Ceramics Using a Biaxially Vibrated Nonrotational Ultrasonic Tool," *CIRP Ann.-Manuf. Technol.*, **42**(1), pp. 375–378.
- [48] Wang, J., Feng, P., and Zhang, J., 2017, "Experimental Investigation on the Effects of Thermomechanical Loading on the Vibrational Stability During Rotary Ultrasonic Machining," *Mach. Sci. Technol.*, **21**(2), pp. 239–256.
- [49] Lv, D., Zhang, Y., and Peng, Y., 2016, "High-Frequency Vibration Effects on Hole Entrance Chipping in Rotary Ultrasonic Drilling of BK7 Glass," *Ultrasonics*, **72**, pp. 47–56.
- [50] Jiao, F., 2008, "The Theoretical and Experimental Studies on Ultrasonic Aided High Efficiency Lapping With Solid Abrasive of Engineering Ceramic," Ph.D. thesis, Shanghai Jiao Tong University, Shanghai, China.
- [51] Marshall, D. B., and Abdalla, H. S., 1980, "Elastic/Plastic Indentation Damage in Ceramics: The Medial Radial Crack System," *J. Am. Ceram. Soc.*, **63**(9–10), pp. 574–581.
- [52] Nath, C., Lim, G. C., and Zheng, H. Y., 2012, "Influence of the Material Removal Mechanisms on Hole Integrity in Ultrasonic Machining of Structural Ceramics," *Ultrasonics*, **52**(5), pp. 605–613.